catalysts

MDPI

Article

In Situ Metallic Bi-Modified (110)BiOBr Nanosheets with Surface Plasmon Resonance Effect for Enhancing Photocatalytic Performance Despite of Larger Optical Band Gap

Yunhe Mu [1,2], Hongxue Chu [1,2], Hougang Fan [1,2,3,*], Xin Li [1,2,3], Xiaoyan Liu [1,2,3], Lili Yang [1,2,3], Maobin Wei [1,2,3,*] and Huilian Liu [1,2,3]

1 College of Physics, Jilin Normal University, Siping 136000, China; xlwl@jlnu.edu.cn (X.L.); liuxiaoyan1437@163.com (X.L.); llyang1980@126.com (L.Y.); lhl541@jlnu.edu.cn (H.L.)
2 Key Laboratory of Functional Materials Physics and Chemistry of the Ministry of Education, Jilin Normal University, Changchun 130103, China
3 National Demonstration Centre for Experimental Physics Education, Jilin Normal University, Siping 136000, China
* Correspondence: fanhougang@jlnu.edu.cn (H.F.); njtyjs4@jlnu.edu.cn (M.W.)

Abstract: BiOBr with different preferred growth orientation facets would show a different photocatalytic performance. When decorated in situ with metallic Bi nanoparticles, Bi/BiOBr would commonly display an enhanced photocatalytic performance. In this paper, the BiOBr nanoplates with preferred growth orientation (102) facet and (110) facet were first synthesized using a hydrothermal method. Then, some metallic Bi nanoparticles were modified in situ onto the (110)BiOBr nanoplates, which was expected to show a much more enhanced photocatalytic performance. All samples were characterized using XRD, FE-SEM, TEM, N_2 adsorption–desorption, UV–vis and XPS. FE-SEM and TEM images showed that the grain size of the metallic Bi particles was about 5 nm to 10 nm. UV–vis spectra showed that, after some metallic Bi nanoparticles were modified on (110)BiOBr nanoplates, the light absorbance in the visible light region at 400–700 nm became stronger and their optical band gap became larger. N_2 adsorption–desorption tests showed that the Bi(x)/(110)BiOBr nanosheets possessed larger specific surface areas than that of the (102)BiOBr and (110)BiOBr nanoplates. The XPS results showed that Bi(x)/(110)BiOBr contained more oxygen vacancies and a more negative value of the conduction band minimum. The photocatalytic performance of (102)BiOBr, (110)BiOBr and Bi(x)/(110)BiOBr were tested in the photocatalytic degradation of rhodamine B under visible light irradiation for 2 h; their photocatalytic efficiency was 45%, 75% and 80%, respectively. In comparison to (102)BiOBr, (110)BiOBr exhibited much higher photocatalytic activity, while for Bi(x)/(110)BiOBr, despite the surface Plasmon resonance effect, a larger specific surface area and more oxygen vacancies, the enhancement of the efficiency was limited, which might have resulted from the larger optical band gap.

Keywords: BiOBr; metallic Bi; SPR effect; larger band gap; oxygen vacancy

Citation: Mu, Y.; Chu, H.; Fan, H.; Li, X.; Liu, X.; Yang, L.; Wei, M.; Liu, H. In Situ Metallic Bi-Modified (110)BiOBr Nanosheets with Surface Plasmon Resonance Effect for Enhancing Photocatalytic Performance Despite of Larger Optical Band Gap. *Catalysts* **2024**, *14*, 654. https://doi.org/10.3390/catal14090654

Academic Editor: Detlef W. Bahnemann

Received: 31 July 2024
Revised: 9 September 2024
Accepted: 17 September 2024
Published: 23 September 2024

1. Introduction

Two-dimensional layered structures like graphene [1,2], MoS_2 [3,4] and bismuth-based materials [5,6] have attracted much attention in the last two decades, especially BiOX (X = Cl, Br, I) materials [7–9]. BiOBr is a promising layered photocatalyst with low cost, non-toxicity, high photostability, an appropriate band gap and remarkable exceptional electronic and optical properties, and has great potential application in energy storage and environmental purification [10,11]. However, the high recombination rate of photogenerated electron-hole pair impedes its practical application [9,12,13]. Researchers have spent much effort on compositing BiOBr with other semiconductors [14,15] and dopping other elements on Bi sites

or Br sites [16–19], which could lower the high recombination rate of a photogenerated electron-hole pair to some degree. Some scholars find that BiOBr with (001) exposed facets possesses better photocatalytic performance than that of (110) exposed facets [20–25]. However, the research on the (102) and (110) exposed facets and in situ metallic Bi-decorated on BiOBr with specific exposed facets [26–29] is still far from enough. Some types of artificially synthesized dye produced by printing and dyeing factories are serous pollutants in water and are difficult to be degradated naturally but are easily removed using a semiconductor under sunlight [30]. Among them, rhodamine B (RhB) was regarded as the most difficult to be photodegradated, so RhB was often a target pollutant to test the photocatalytic performance of various materials.

Herein, we first synthesized BiOBr nanoplates under two different temperatures with a hydrothermal method. It was interesting that the preferred growth orientation facets of the two samples were different; one was (102) facet and the other was (110) facet, which were named as (102)BiOBr and (110)BiOBr, respectively. Since (110)BiOBr possessed the better photocatalytic performance, some metallic Bi nanoparticles were in situ modifiedon 2 mmol (110)BiOBr nanoplates to form Bix/(110)BiOBr (x = 0.5 mmol, 1.0 mmol and 1.5 mmol) nanosheets. Usually, the surface Plasmon resonance (SPR) effect resulting from the metallic Bi nanoparticles [27,31,32] greatly enhances the photocatalytic performance of Bix/(110)BiOBr nanosheets; however, we found that it was not the case.

2. Results and Discussion

2.1. Structure and Photocatalytic Performance

Figure 1A showed the XRD patterns of standard BiOBr peaks and the two prepared BiOBr samples under different hydromel synthesis temperatures. The (102)BiOBr and (110)BiOBr samples displayed almost the same diffraction peaks without any other impurity peaks. The six sharp diffraction peaks located at 10.84°, 25.15°, 31.68°, 32.25°, 46.20° and 57.14° could be attributed to the (001), (101), (102), (110), (200) and (212) facets through the standard BiOBr phase (JCPDS number: 09-0393); their lattice constants are listed in Table S1. The significant difference between the two samples was that the strongest peak was (102) facets and (110) facets, respectively, which implied that the preferred growth orientation was different in (102)BiOBr and (110)BiOBr. In Figure 1B, after in situ decoration with different amount of metallic Bi nanoparticles, the three Bix/(110)BiOBr samples show no peaks of any impurities but three peaks of the metallic Bi (JCPDS number: 05-0519). The metallic Bi could form in situ on the surface of the (110)BiOBr sample in the hydrothermal synthesis process under the reduction in $Bi(NO_3)_3 \bullet 5H_2O$ by glycol.

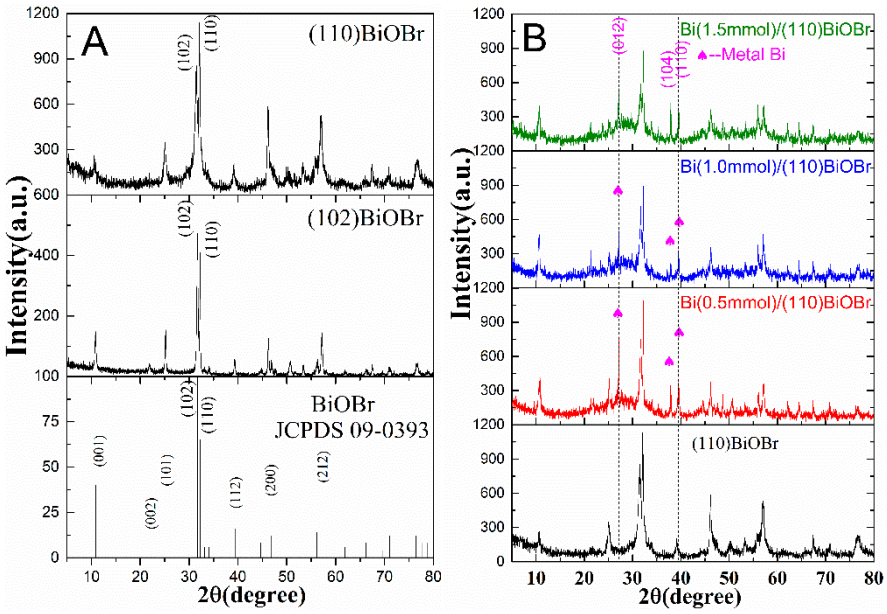

Figure 1. XRD pattern of (**A**) the (102)BiOBr and (110)BiOBr samples, (**B**) Bix/(110)BiOBr samples.

Figures 2A,B, S1 and S2 show the morphology and element mapping of (102)BiOBr and (110)BiOBr; both were nanoplates about 300–600 nm width and no obvious difference could be observed. After in situ decoration with different amounts of metallic Bi nanoparticles, the morphology of Bi/(110)BiOBr changed from stacked nanoplates to stacked nanosheets, as shown in Figure 2C–E. As shown in Figures S3–S5, in the three Bix/(110)BiOBr samples, the Bi, Br and O elements were evenly distributed. The presence of metallic Bi nanoparticles can be clearly observed in Figure 2G,H. The grain size of the metallic Bi particles was about 5 nm to 10 nm.

Figure 3A,B shows the photocatalytic performance of degradating the RhB of the above five samples under visible light. After being in darkness for 30 min, the concentration of RhB decreased to 97%, 67%, 87%, 82% and 78% for (102)BiOBr, (110)BiOBr and the three Bix/(110)BiOBr samples, respectively. After 2 h visible light irradiation, about 45.1% and 75.2% of RhB were photocatalytically degradated using the (102)BiOBr sample and the (110)BiOBr sample, respectively. As shown in Figure 3B, the photocatalytic performances of the three Bix/(110)BiOBr samples were 79.0%, 80.8% and 79.2%, respectively, which were all better than that of the (110)BiOBr sample, as expected; the improvement was also not notable, as expected. Since the specific surface area, the optical band gap and the amount of oxygen vacancy would affect the photocatalytic performance of removing RhB, we study the above factors to clarify the difference in the photocatalytic performances among the five samples.

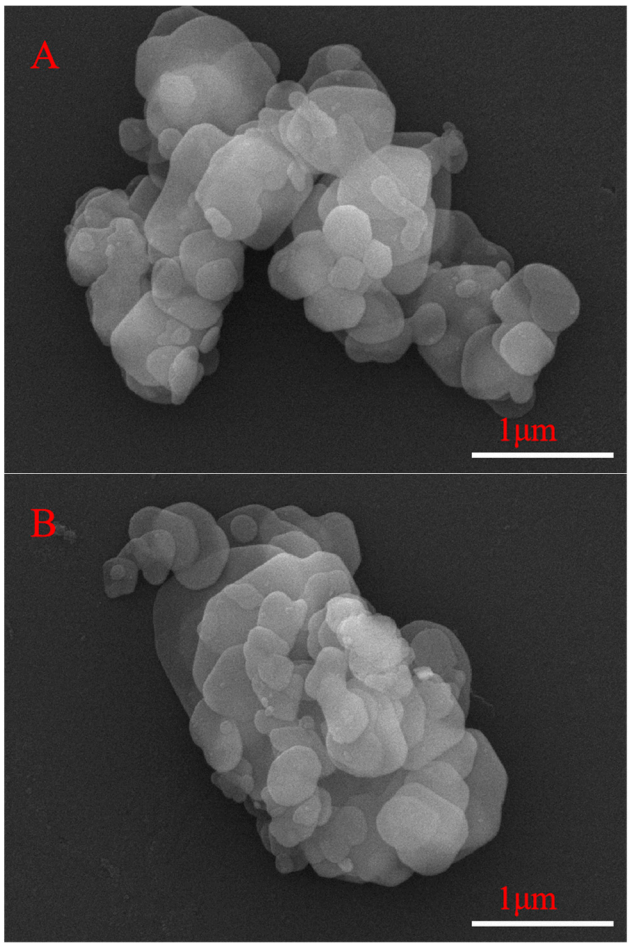

Figure 2. *Cont.*

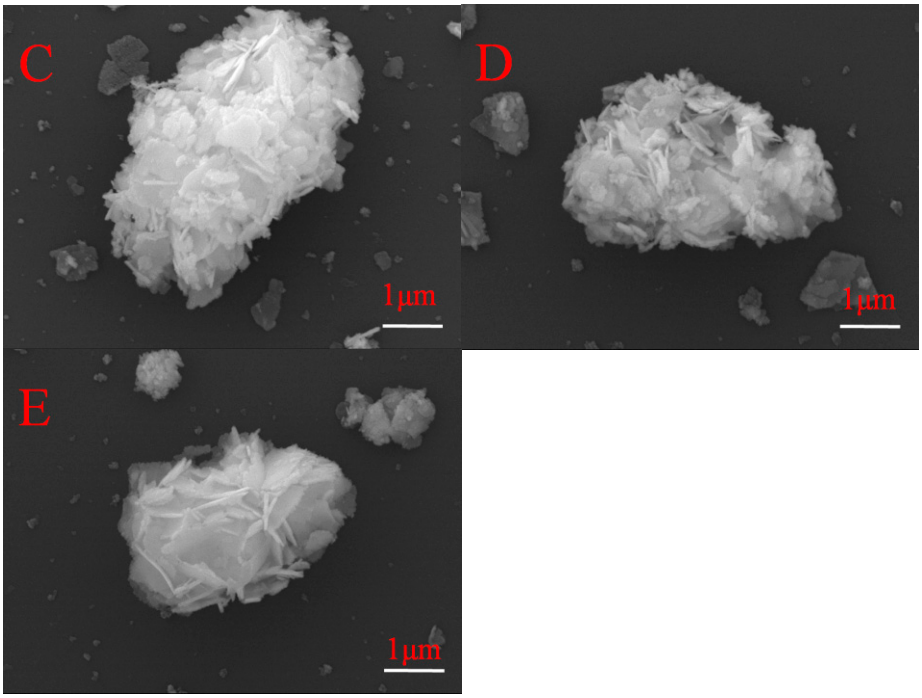

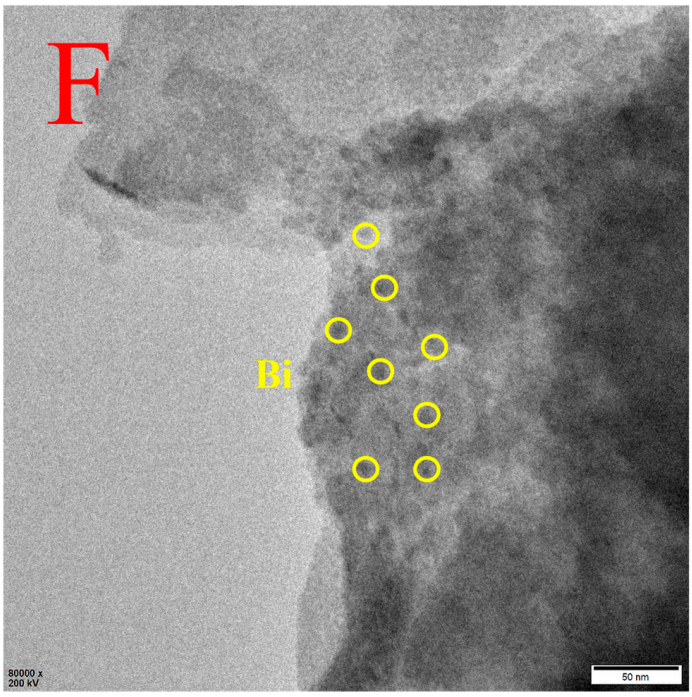

Figure 2. *Cont*.

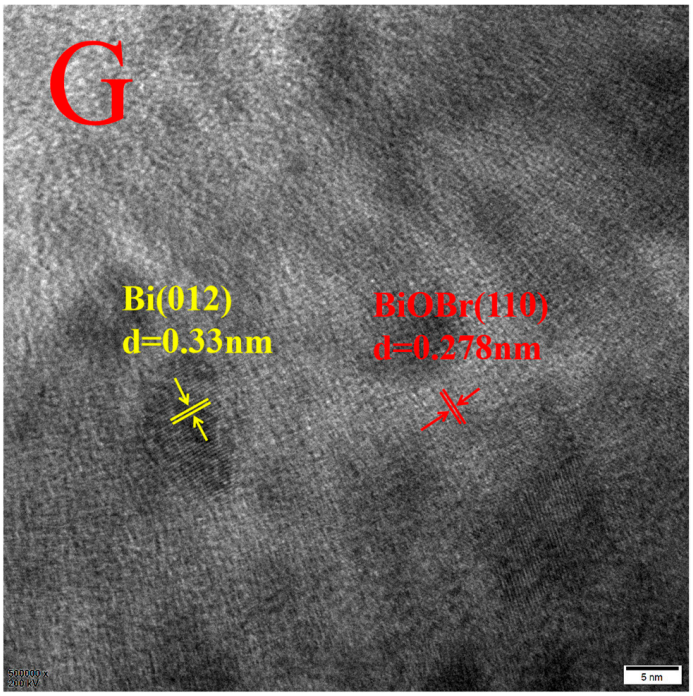

Figure 2. SEM images of (**A**) (102)BiOBr, (**B**) (110)BiOBr, (**C**) Bi(0.5 mmol)/(110)BiOBr, (**D**) Bi (1.0 mmol)/(110)BiOBr, (**E**) Bi(1.5 mmol)/(110)BiOBr and TEM images of (**F**), (**G**) Bi(1.0 mmol)/ (110)BiOBr.

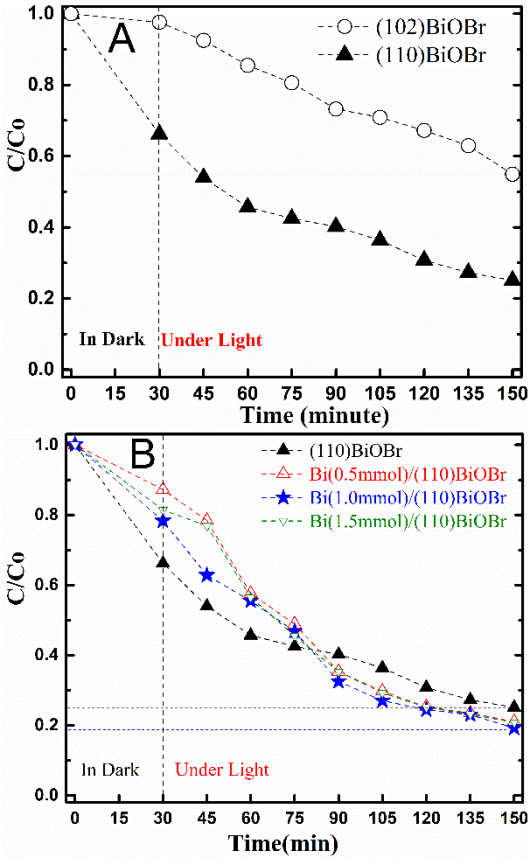

Figure 3. The photocatalytic performance of removing RhB using (**A**) the (102)BiOBr and (110)BiOBr samples, (**B**) Bix/(110)BiOBr samples.

Figure 4A shows N_2 adsorption–desorption isotherms of (102)BiOBr and (110)BiOBr. Both samples exhibited reversible type III isotherms with H2-type hysteresis loops [33,34]. As shown in Figure S7, their pore diameter distribution histograms displayed no obvious difference. The specific surface areas of the two samples are 9.7021 and 14.2066 m^2/g, respectively (listed in Table S2). Usually, the greater the specific surface area, the greater the active site; thus, (110)BiOBr would possess a higher photocatalytic performance in removing RhB than that of (102)BiOBr. For the three Bix/(110)BiOBr samples, they also exhibited reversible type III isotherms with H2-type hysteresis loops and their specific surface areas were 15.8608, 21.2600 and 17.4544 m^2/g, which implied that the three Bix/(110)BiOBr samples would possess higher photocatalytic performances in removing RhB than that of (110)BiOBr.

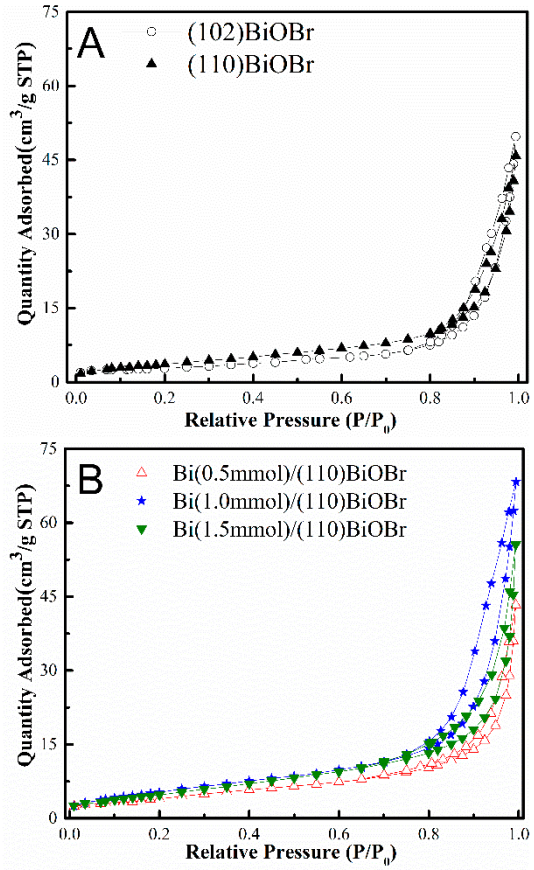

Figure 4. N_2 adsorption–desorption curves of (**A**) (102)BiOBr and (110)BiOBr; (**B**) Bi(0.5 mmol)/(110)BiOBr, Bi(1.0 mmol)/(110)BiOBr and Bi(1.5 mmol)/(110)BiOBr.

2.2. Optoelectronic Performance and Active Species

Figure 5 shows the UV-vis DRS of (102)BiOBr, (110)BiOBr and the three Bix/(110)BiOBr samples. Compared with (102)BiOBr, (110)BiOBr displayed lower absorption in both short wavelength and long wavelength, while its absorption edge was a bit red-shifted, which implied that its optical band gap (Eg) would be smaller. Furthermore, compared with (110)BiOBr, the three Bix/(110)BiOBr displayed lower absorption in the short wavelength but higher absorption in the long wavelength, while the obvious blue-shift of the absorption edges implied that their Eg values would be larger, which might be a result of the quantum confinement effect caused by morphological changes and interfacial interactions between metallic Bi and (110)BiOBr. The Eg values of all the samples were calculated through the Tauc plot and listed in Figure S7 and Table S3. Since the Eg value of (110)BiOBr was smaller than that of (102)BiOBr, it was reasonable to deduce that the (110)BiOBr would display a higher photocatalytic performance in removing RhB than that of (102)BiOBr,

which was in accordance with the previous photocatalytic performance listed in Figure 3. But for the three Bix/(110)BiOBr samples, their Eg values were obviously larger than that of (110)BiOBr; this seemed to conclude that they would display a lower photocatalytic performance in removing RhB than that of (110)BiOBr because of the extreme decrease in the photogenerated electron-hole pairs, which was contrary to the results shown in Figure 3. It could also be clearly observed in Figure 5 that each of the three Bix/(110)BiOBr samples displayed a wider light-absorption enhancement between 400 and 700 nm than that of (102)BiOBr and (110) BiOBr, which resulted from the SPR effect of the metallic Bi nanoparticles [26–28,35,36]. Usually, the SPR effect would promote visible-light absorption to produce more photogenerated electron-hole pairs, resulting in an enhancement of photocatalytic activity [26–28,35,36], which is in accordance with the photocatalytic activity shown in Figure 3.

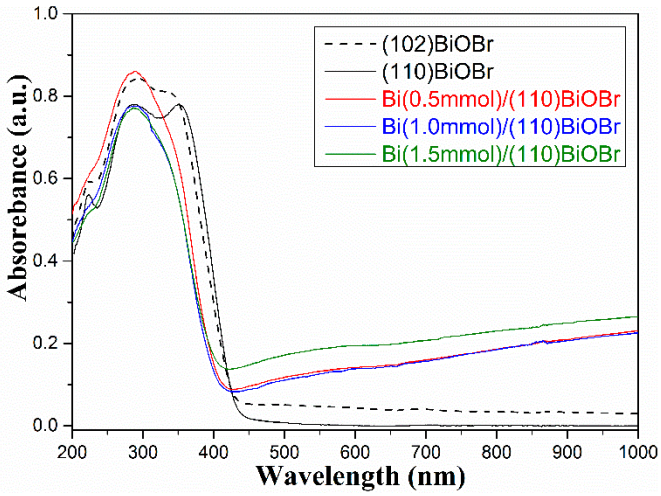

Figure 5. UV-vis absorption spectra of all the samples.

In order to investigate the surface chemical states and the amount of oxygen vacancy, we conducted XPS measurement on the (102)BiOBr, (110)BiOBr and Bi(1.0 mmol)/(110)BiOBr samples. Figures 6A–C and S8 showed the XPS spectra and the high resolution XPS scanned over Bi-4f, Br-3d, O-1s and C-1s peaks of the selected three samples, which clearly demonstrated the existence of Bi^{3+}, Br^{-} [28,36]. The deconvolution of the O-1s peaks of the three samples is listed in Figure 6D–F; the three peaks around 530.0 eV, 531.5 eV and 532.5 eV corresponded to the lattice oxygen (O_L), oxygen vacancy (O_V) and the absorbed oxygen (O_A), respectively [26–28,36]. Their peak area percentages of O_L, O_V, and O_A were calculated and listed in Table 1. O_V always played a dominant role in the photocatalytic process because O_V would become a trap to attract photogenerated electrons, which would be beneficial for the separation of the photogenerated electron-hole pairs [26,27,36–38]. Usually, the greater the amount of O_V, the better the photocatalytic performance will be. However, we can clearly see in Table 1 that the proportion of O_V in the (102)BiOBr sample (16%) was a bit larger than that in the (110)BiOBr sample (14%), while the proportion of O_V in the Bi (1.0 mmol)/(110)BiOBr sample was 19%.

Figure 7A showed the photocurrents of the five samples. After alternating on or off lights every 20 s for 160 s, the photocurrents of the (102)BiOBr sample and (110)BiOBr sample were about 2.13 μA and 3.11 μA; the three Bix/(110)BiOBr samples were 3.44 μA, 9.04 μA and 6.82 μA, respectively. Apparently, the photocurrent of the (110)BiOBr sample was larger than that of the (102)BiOBr sample and the photocurrents of the three Bix/(110)BiOBr samples were all larger than that of the (110)BiOBr sample. Usually, the lower the recombination rate of the photogenerated electron-hole pairs is, the higher the photocurrent will be. Since the Bi(1.0 mmol)/(110)BiOBr sample possessed the SPR effect as well as the highest amount of O_V, it displayed the highest photocurrent value.

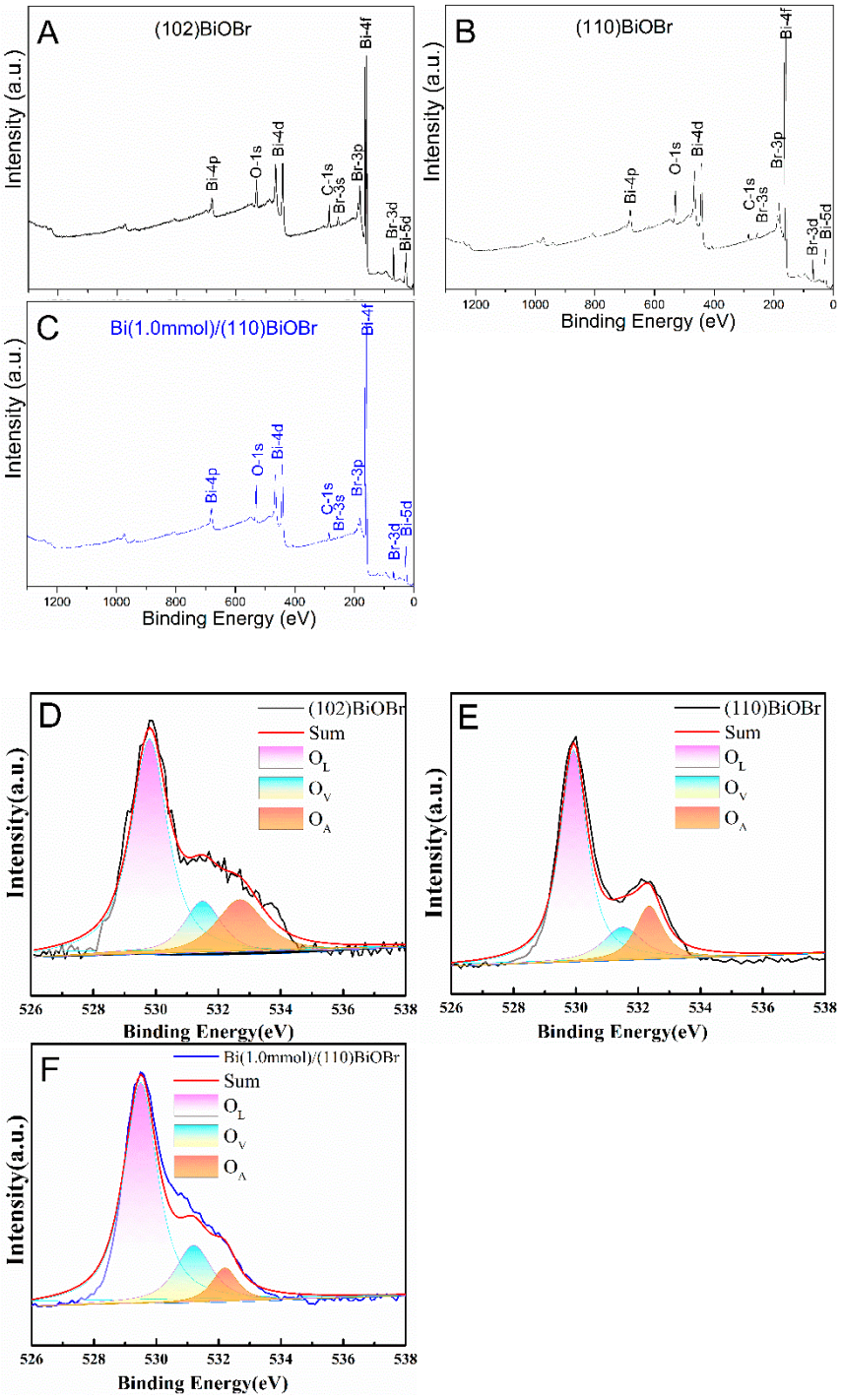

Figure 6. (**A**–**C**) XPS spectra of the selected three samples and (**D**–**F**) the deconvolution results of the selected three samples in high resolution O 1s XPS spectra.

Table 1. The peak area percentages of the selected three samples in high resolution XPS spectra.

	O_L	O_V	O_A
(102)BiOBr	65%	16%	19%
(110)BiOBr	68%	14%	18%
Bi(1.0 mmol)/(110)BiOBr	65%	19%	16%

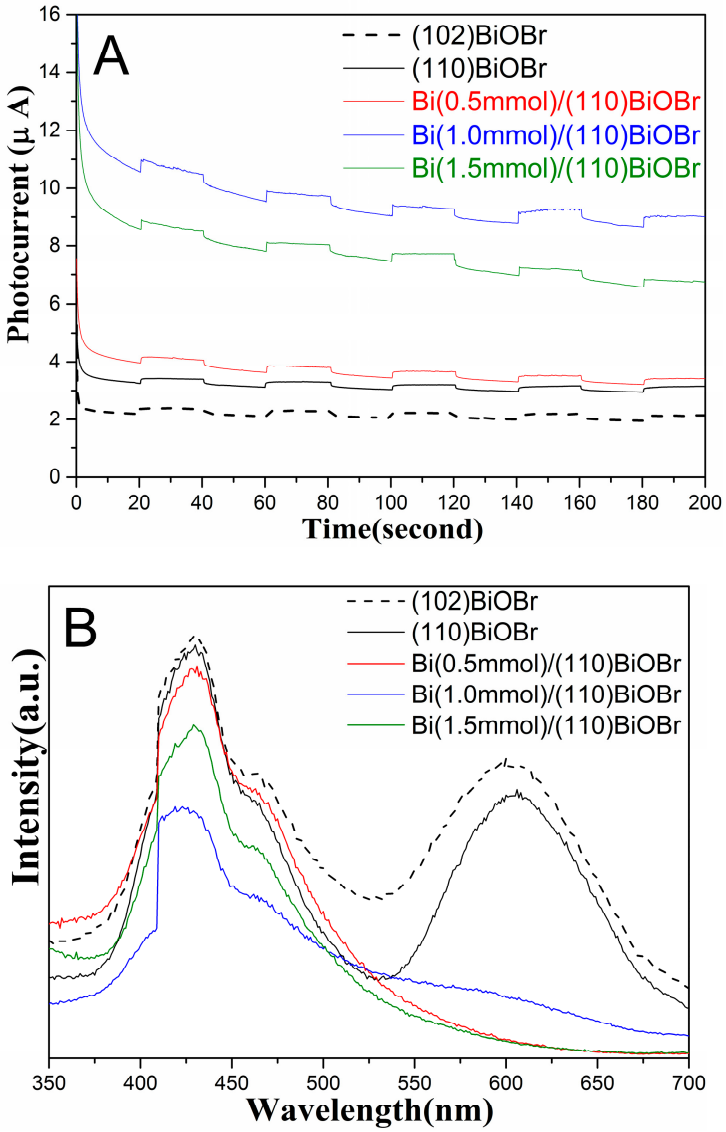

Figure 7. (**A**) The photocurrents and (**B**) PL spectra of all the samples.

To investigate the separation efficiency of the photogenerated electron-hole pair, we presented the PL spectra in Figure 7B. For all the samples, the peak around 425 nm could be attributed to the intrinsic excitation of BiOBr, while the broadened peak from 550 nm to 675 nm for (102)BiOBr and (110)BiOBr could be attributed to the impurity excitation [8,10]. It was clear that the ranking of the PL intensity for the five samples was (102)BiOBr, (110)BiOBr, Bi(0.5 mmol)/(110)BiOBr, Bi(1.5 mmol)/(110)BiOBr and Bi(1.0)/(110)BiOBr, in which the trend was contrary to that of the photocatalytic performance of removing Rh B in Figure 3 and the photocurrent in Figure 7A. Since the PL intensity was closely related to the recombination rate of the photogenerated electron-hole pairs, the higher the recombination rate was, the larger the PL intensity would be, but the worse the photocatalytic performance would be.

To probe the active species in the photocatalytic process, we tested the photocatalytic removal of RhB with different scavengers for the selected three samples shown in Figure 8. It was obvious that the main active species was superoxide radical ($\cdot O_2^-$) for the selected three samples, with a few of the other three active species: photogenerated electrons (e^-), photogenerated holes (h^+) and hydroxyl radicals ($\cdot OH$).

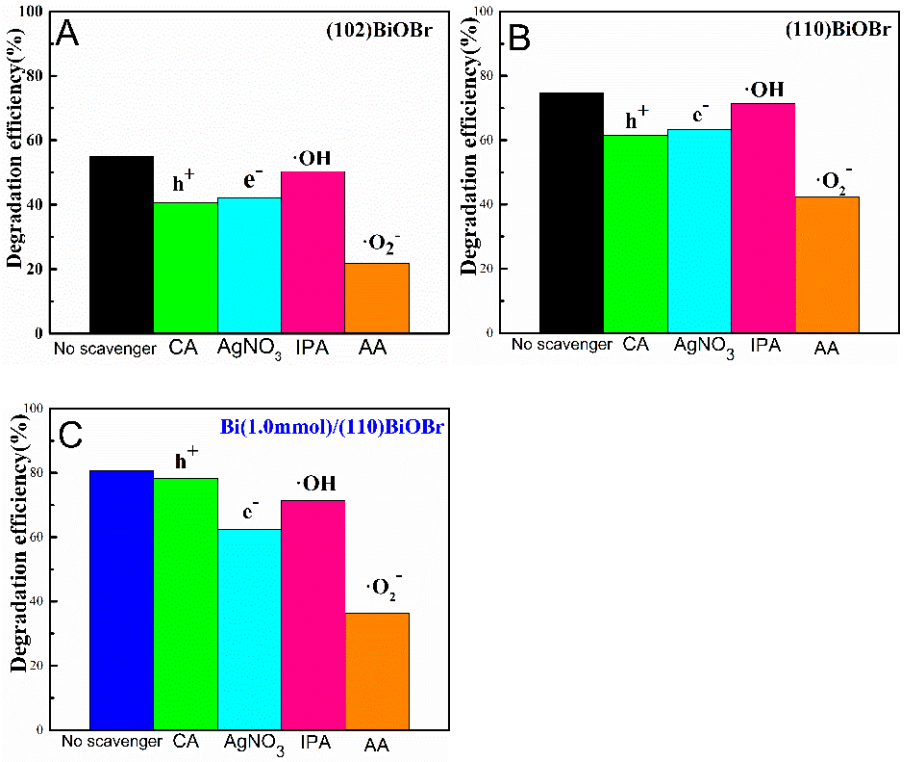

Figure 8. Photocatalytic removal of RhB with four scavengers by (**A**) (102)BiOBr, (**B**) (110)BiOBr and (**C**) Bi(1.0mmol)/(110)BiOBr.

2.3. Photocatalytic Mechanism

To clarify the reason for the difference in the photocatalytic performance of removing Rh B using the five samples, we split them into two groups, of which we will explain them one by one; the first group consists of the (110)BiOBr and (102)BiOBr samples, and the second group consists of four samples, the (110)BiOBr and the three Bix/(110)BiOBr samples. For the first group, the (110)BiOBr sample possessed a larger specific surface area, smaller Eg and a slightly smaller amount of oxygen vacancy than that of the (102)BiOBr sample. Usually, the larger specific surface area and the smaller are the two main positive factors for the enhancement of photocatalytic performance, while the smaller amount of oxygen vacancy is the main negative factor for the enhancement of the photocatalytic performance. Since the amount of oxygen vacancy in the (110)BiOBr sample was only a bit smaller than that in the (102)BiOBr sample, this negative factor would only result in a slight decrease in the photocatalytic performance. The overall outcome between the two main positive factors and one minor negative factor was that the (110)BiOBr sample could photocatalytically remove 75.2% of RhB while the (102)BiOBr sample could only photocatalytically remove 45.1% of RhB.

For the second group, the Eg of the three Bix/(110)BiOBr samples was 3.18 eV, 3.18 eV and 3.19 eV, respectively, which were all obviously larger than that of the (110)BiOBr sample (3.05 eV). Usually, a much larger Eg is a huge negative factor for the photocatalytic performance of removing Rh B. The specific surface area of the three Bix/(110)BiOBr were all larger than that of the (110)BiOBr sample, which was a positive factor for photocatalytic performance. The amount of oxygen vacancy of the Bi(1.0 mmol)/(110)BiOBr sample (19%) was obviously larger than that of the (110)BiOBr sample (14%), which would be a notable positive factor for photocatalytic performance. The SPR effect shown in Figure 5 was also a notable positive factor. So, after the competition between the one negative factor and three positive factors, the photocatalytic performance of the three Bi/(110)BiOBr samples was only enhanced to about 80%, which was only a bit better than that of the (110)BiOBr sample, as shown in Figure 3. As for the three Bix/(110)BiOBr samples, they showed almost the

same morphology and Eg; the differences in their specific surface area were so small that they showed almost the same photocatalytic performance of the removal RhB resulting from the SPR effect.

Figure 9 displayed the structure of BiOBr nanosheets with decorated metallic Bi nanoparticles. When irradiated under visible light, the BiOBr nanosheets would produce photogenerated electron-hole pairs; the photogenerated electron would transfer from BiOBr nanosheets to the metallic Bi nanoparticles and then react with oxygen to generate superoxide radical ($\cdot O_2^-$) to photocatalytically remove RhB.

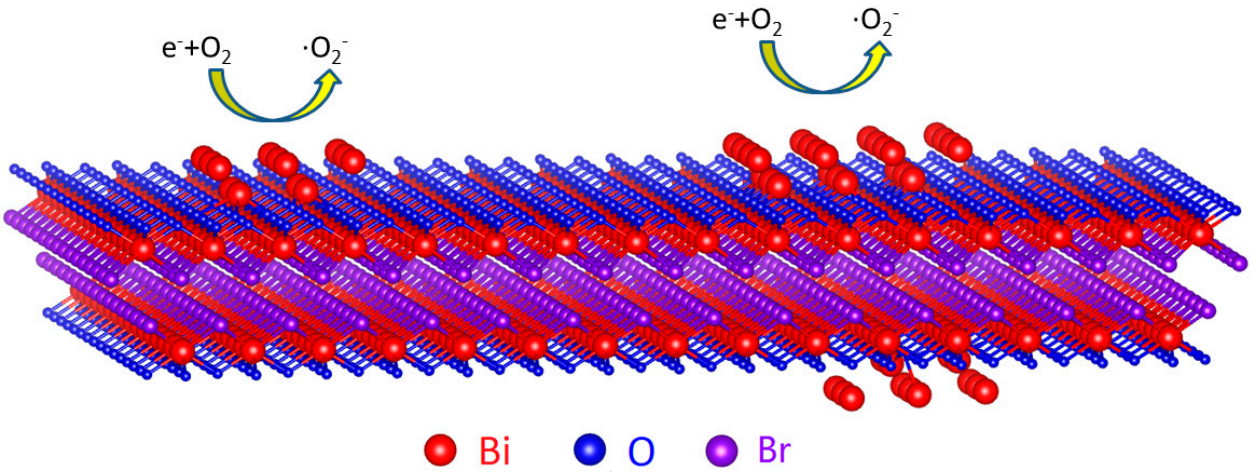

Figure 9. The schematic diagram of the role of the SPR effect between metallic Bi and BiOBr.

Figure 10 showed the energy level of (102)BiOBr, (110)BiOBr and Bi(1.0 mmol)/(110)BiOBr. Their position in the valence band maximum was obtained through XPS data in Figure S9 and listed in Table S4, while the position of the conduction band minimum could be calculated by adding the Eg to the value of the above valence band maximum. For (102)BiOBr and (110)BiOBr, the Eg of the latter was smaller than that of the former, so more photogenerated electrons were produced and reacted with oxygen to form superoxide radical ($\cdot O_2^-$). For (110)BiOBr and Bi(1.0 mmol)/(110)BiOBr, though the latter possessed a larger Eg, the metallic Bi would attract the photogenerated electrons and facilitate the transfer and separation of the photogenerated electron-hole pairs, which eventually would enhance the photocatalytic performance. As for the main species in the photocatalytic process, the photogenerated electrons would shift down to the level of 0.33 eV and react with oxygen to form superoxide radical ($\cdot O_2^-$). But the photogenerated holes (h^+) would hardly shift down to the level of 2.38 eV or 2.40 eV or react with H_2O or OH^- to form hydroxyl radicals (·OH). The mobility of the photogenerated hole (h^+) was much lower than that of the photogenerated electron. So, the main species in the above photocatalytic process was superoxide radical ($\cdot O_2^-$) with a minor amount of photogenerated electrons (e^-), photogenerated holes (h^+) and hydroxyl radicals (·OH). The corresponding reaction equations are listed below:

$$Bi/BiOBr + hv = h^+ + e^- \quad (1)$$

$$e^- + O_2 = \cdot O_2^- \quad (2)$$

$$\cdot O_2^- + RhB = CO_2 + H_2O + \text{other inorganic compound} \quad (3)$$

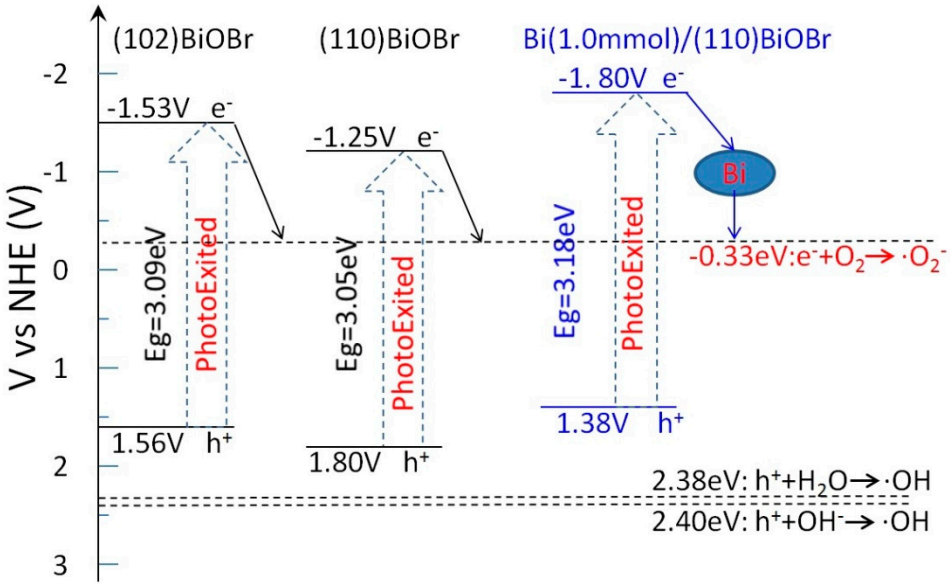

Figure 10. The schematic diagram of energy level and the photogenerated electrons transfer of the selected three samples.

3. Materials and Methods

3.1. Materials

The starting materials, bismuth nitrate pentahydrate ($Bi(NO_3)_3{\cdot}5H_2O$, ≥99.0%), potassium bromide (KBr, ≥99.0%), anhydrous ethanol (CH_3CH_2OH, ≥99.7%), ethylene glycol ($HOCH_2CH_2OH$, ≥99.5%) and rhodamine B (RhB), all of them were AR grade and purchased from Sinopharm Chemical Reagent Co., Ltd. (Shanghai, China). All the chemical materials in the experiment were used without any further purification.

3.2. Preparation of (102)BiOBr and (110)BiOBr

The (102)BiOBr and (110)BiOBr nanoplates were synthesized using a one-step hydrothermal method. In a typical synthesis, 1.5 mmol KBr was placed in 16 mL of anhydrous ethanol, which was then transferred to an ultrasonic cleaner and dispersed for 10 min. Then, at room temperature, the same stoichiometric $Bi(NO_3)_3{\cdot}5H_2O$ was slowly put into the above dispersion and magnetically stirred for 2 h. The mixture was then poured into a stainless steel autoclave, sealed and heated at 180 °C ((102)BiOBr) and 140 °C((110)BiOBr) for 12 h, respectively. The stainless steel autoclave was then naturally cooled to room temperature. The resulting precipitate was collected using centrifugation and washed several times with deionized water and ethanol. Finally, it was dried in a drying oven at 60 °C for 12 h and some light yellow powder was obtained.

3.3. Preparation of Bi/(110)BiOBr

The (110)BiOBr nanoplates decorated with different amounts of metallic Bi, Bix/(110)BiOBr/(x = 0.5 mmol, 1.0 mmol and 1.5 mmol) samples were also prepared using the hydrothermal method. First, under the condition of ultrasonic dispersion, the prepared 2 mmol (110)BiOBr sample was added to 80 mL glycol, and a certain amount of $Bi(NO_3)_3{\cdot}5H_2O$ (0.5 mmol, 1 mmol, 1.5 mmol) was added to the solution for 2 h via magnetic stirring and stirred magnetically for 10 min. The mixture was poured into a stainless steel autoclave, sealed and heated at 180 °C for 10 h; then, the stainless steel autoclave was naturally cooled to room temperature, the resulting precipitate was collected using centrifugation, washed several times with deionized water and ethanol and finally dried in a drying oven at 60 °C to obtain some gray-black powder.

3.4. Material Characterization

The crystal structure of all the samples was determined using X-ray diffraction (XRD, MXP18, MAC Science, Tokyo, Japan). The morphology of all the samples was characterized using scanning electron microscopy (SEM, JSM-7800F, Japanese Hitachi, Tokyo, Japan). The UV-vis diffuse reflectance absorption (UV-vis DRS) spectra were acquired with an UV-vis spectrophotometer (UV-5800PC, Shanghai Metash Instruments Co., Ltd., Shanghai, China). N_2 adsorption–desorption isotherms were recorded using a BET test system (ASAP 2460, Mike Co., Ltd., Columbus, OH, USA). To probe the recombination rate of the photogenerated electron-hole pairs, the photoluminescence (PL) spectra were recorded (FLS1000, Edinburgh Instruments Co., Ltd., Edinburgh, UK).

The photoelectrochemical properties were characterized using a computer-controlled CHIe660C electrochemical workstation (Shanghai Chenhua Co., Shanghai, China) with a standard three-electrode system. The saturated calomel electrode (SCE) and platinum mini grid were used as the reference electrode and counter electrode, respectively. When measuring the photocurrents, the working electrode was a pretreated indium tin oxide (ITO) glass coated with the sample to be tested. The supporting electrolyte was 0.5 M Na_2SO_4 solution, the applied potential was 0.05 V and a 300 W Xe lamp was used as the excitation light source.

3.5. Photocatalytic Testing

The photocatalytic performance was evaluated using the photodegradation of RhB in aqueous solution. A 50 mg photocatalyst was dispersed into a solution of 100 mL pollutants (RhB~5 mg/L) and stirred in the dark for 30 min to reach the adsorption–desorption equilibrium. The mixture was then exposed to visible light. The visible light source was a halogen lamp (300 W, $\lambda > 420$ nm). During the whole photocatalytic test, a certain height was maintained between the light source and the liquid surface of the solution. At specified intervals, 3 mL of the solution was drawn through a syringe and the photocatalyst was removed with a strainer plug. Then, the residual concentrations of RhB were determined using UV-visible spectrophotometer (Shanghai Metash Instruments Co., Ltd., UV-5800PC, Shanghai, China). The scavenging tests were performed according to the above experimental procedure for the (102)BiOBr, (110)BiOBr, (110)BiOBr and Bi(1.0)/(110)BiOBr samples. Isopropyl alcohol(IPA), ascorbic acid (AA), potassium bromate (PB) and citric acid (CA) were added to the reaction solution as scavengers for hydroxyl radicals (·OH), superoxide radicals ($\cdot O_2^-$), electron (e^-) and photogenerated- holes (h^+), respectively.

4. Conclusions

In summary, the (110)BiOBr owes its much better photocatalytic performance, compared to that of (102)BiOBr, to its smaller Eg and larger specific surface area, despite its smaller amount of oxygen vacancy. When decorated with metallic Bi nanoparticles, despite the negative influence of the larger Eg, the Bix/(110)BiOBr samples still has a larger specific surface area and a greater amount of oxygen vacancy than that of (110)BiOBr; together with the SPR effect as a result of the metallic Bi, their recombination rates of photogenerated electron-hole pairs become lower, which eventually enhances their photocatalytic performance. These efficient BiOBr-based catalysts would be suitable candidates in water treatment, removing organic pollutants to ensure a sustainable and green environment. Since the conduction band minimum of BiOBr is higher than −1 eV, the BiOBr-based catalysts might be suitable for CO_2 photoreduction into CO and other chemicals.

Supplementary Materials: The following supporting information can be downloaded at: https://www.mdpi.com/article/10.3390/catal14090654/s1, Table S1: The lattice constants of all the samples; Figure S1: Element Mapping of the (102)BiOBr sample; Figure S2: Element Mapping of the (110)BiOBr sample; Figure S3: Element Mapping of the Bi(0.5mmol)/(110)BiOBr sample; Figure S4: Element Mapping of the Bi(1.0mmol)/(110)BiOBr sample; Figure S5: Element Mapping of the Bi(1.5mmol)/(110)BiOBr sample; Figure S6: The pore diameter distribution of all the samples; Table S2:The BET specific surface

area of all the samples; Figure S7: The optical band gap(Eg) of all the samples through Tauc plot; Table S3: The optical Gap (Eg) of all the samples; Figure S8: Bi-4f, Br-3d, O-1s and C-1s of the three samples; Figure S9:The valence band maximum of the three samples; Table S4: The valence band maximum of the selected thee samples obtained from Figure S9.

Author Contributions: Y.M.: investigation, data curation, writing—original draft. H.C.: data curation, visualization. H.F.: conceptualization, writing—review and editing, formal analysis. X.L. (Xin Li): software, formal analysis. X.L. (Xiaoyan Liu): validation, formal analysis. L.Y.: conceptualization, methodology. M.W.: resources, formal analysis. H.L.: supervision, resources. All authors have read and agreed to the published version of the manuscript.

Funding: This research was funded by the Program for the Development of Science and Technology of Jilin Province (Item No. 20220402031GH, YDZJ202301ZYTS246), the National Natural Science Foundation of China (No. 22075101) and the Program for the Science and Technology of Education Department of Jilin Province (Item No. JJKH20220441KJ).

Data Availability Statement: All relevant data are within the manuscript and its additional files. The data are available from the corresponding author on reasonable request.

Conflicts of Interest: The authors declare that they have no known competing financial interests or personal relationships that could have appeared to influence the work reported in this paper.

References

1. Novoselov, K.S.; Geim, A.K.; Morozov, S.V.; Jiang, D.; Katsnelson, M.I.; Grigorieva, I.V.; Dubonos, S.V.; Firsov, A.A. Two-dimensional gas of massless Dirac fermions in graphene. *Nature* **2005**, *438*, 197–200. [CrossRef] [PubMed]
2. Zhang, Y.; Tan, Y.-W.; Stormer, H.L.; Kim, P. Experimental observation of the quantum Hall effect and Berry's phase in graphene. *Nature* **2005**, *438*, 201–204. [CrossRef]
3. Pham, P.V.; Mai, T.-H.; Do, H.-B.; Vasundhara, M.; Nguyen, V.-H.; Nguyen, T.; Bui, H.V.; Dao, V.-D.; Gupta, R.K.; Ponnusamy, V.K.; et al. Layer-by-layer thinning of two-dimensional materials. *Chem. Soc. Rev.* **2024**, *53*, 5190–5226. [CrossRef] [PubMed]
4. Liu, L.; Liu, N.; Chen, B.; Dai, C.; Wang, N. Recent Modification Strategies of MoS_2 towards Electrocatalytic Hydrogen Evolution. *Catalysts* **2024**, *14*, 126. [CrossRef]
5. Kang, Z.; Lin, E.; Qin, N.; Wu, J.; Yuan, B.; Bao, D. Effect of oxygen vacancies and crystal symmetry on piezocatalytic properties of Bi_2WO_6 ferroelectric nanosheets for wastewater decontamination. *Environ. Sci. Nano* **2021**, *8*, 1376–1388. [CrossRef]
6. Li, J.; Zhang, W.; Ran, M.; Sun, Y.; Huang, H.; Dong, F. Synergistic integration of Bi metal and phosphate defects on hexagonal and monoclinic $BiPO_4$: Enhanced photocatalysis and reaction mechanism. *Appl. Catal. B Environ.* **2019**, *243*, 313–321. [CrossRef]
7. Mishra, S.; Acharya, L.; Marandi, B.; Sanjay, K.; Acharya, R. Boosted photocatalytic accomplishment of 3D/2D hierarchical structured $Bi_4O_5I_2$/g-C_3N_4 p-n type direct Z-scheme heterojunction towards synchronous elimination of Cr(VI) and tetracycline. *Diam. Relat. Mater.* **2024**, *142*, 110834. [CrossRef]
8. Wang, Z.; Liu, C.; Chen, F.; Chen, R. Self-Assembly of Porous Hierarchical BiOBr Sub-Microspheres for Efficient Aerobic Photooxidation of Benzyl Alcohol under Simulated Sunlight Irradiation. *Catalysts* **2023**, *13*, 958. [CrossRef]
9. Alapi, T.; Veres, B.; Náfrádi, M.; Farkas, L.; Pap, Z.; Covic, A. Application of BiOX Photocatalyst to Activate Peroxydisulfate Ion-Investigation of a Combined Process for the Removal of Organic Pollutants from Water. *Catalysts* **2023**, *13*, 513. [CrossRef]
10. Liu, D.; Chen, D.; Li, N.; Xu, Q.; Li, H.; He, J.; Lu, J. Surface Engineering of g-C_3N_4 by Stacked BiOBr Sheets Rich in Oxygen Vacancies for Boosting Photocatalytic Performance. *Angew. Chem. Int. Ed.* **2020**, *59*, 4519–4524. [CrossRef]
11. Qi, Y.; Zhao, S.; Jiang, X.; Kang, Z.; Gao, S.; Liu, W.; Shen, Y. Visible-Light-Driven BiOBr-TiO_2-Attapulgite Photocatalyst with Excellent Photocatalytic Activity for Multiple Xanthates. *Catalysts* **2023**, *13*, 1504. [CrossRef]
12. Chen, G.; Li, Y.; Liu, B.; Miao, Y. Recent developments in bismuth oxyhalide-based functional nanomaterials for biomedical applications. *Biomater. Sci.* **2022**, *10*, 5809–5830. [CrossRef] [PubMed]
13. Liu, J.; Guo, H.; Yin, H.; Nie, Q.; Zou, S. Accelerated Photodegradation of Organic Pollutants over BiOBr/Protonated g-C_3N_4. *Catalysts* **2022**, *12*, 1109. [CrossRef]
14. Wang, M.; Osella, S.; Brescia, R.; Liu, Z.; Gallego, J.; Cattelan, M.; Crisci, M.; Agnoli, S.; Gatti, T. 2D MoS_2/BiOBr van der Waals heterojunctions by liquid-phase exfoliation as photoelectrocatalysts for hydrogen evolution. *Nanoscale* **2023**, *15*, 522–531. [CrossRef]
15. He, D.; Cao, D.; Ben, C.; Lan, Y.; Zhang, H.; Jiang, M.; Wu, S.; Zhang, Y.; Meng, Q.B.; Song, X.-M. Ionic liquid gel microspheres as an emerging platform for constructing liquid compartment microreactors. *Green Chem.* **2022**, *24*, 5952–5964. [CrossRef]
16. Cai, Z.; Lei, S.; Hu, Y.; Chen, Y.; Shen, M.; Lei, M. Iron doped BiOBr loaded on carbon spheres for improved visible-light-driven detoxification of 2-chloroethyl sulfide. *Dalton Trans.* **2023**, *52*, 3040–3051. [CrossRef]
17. Jin, Y.; Li, F.; Li, T.; Xing, X.; Fan, W.; Zhang, L.; Hu, C. Enhanced internal electric field in S-doped BiOBr for intercalation, adsorption and degradation of ciprofloxacin by photoinitiation. *Appl. Catal. B Environ.* **2022**, *302*, 120824. [CrossRef]

18. An, W.; Wang, H.; Yang, T.; Xu, J.; Wang, Y.; Liu, D.; Hu, J.; Cui, W.; Liang, Y. Enriched photocatalysis-Fenton synergistic degradation of organic pollutants and coking wastewater via surface oxygen vacancies over Fe-BiOBr composites. *Chem. Eng. J.* **2023**, *451*, 138653. [CrossRef]
19. Zhou, S.; Shi, T.; Chen, Z.; Kilin, D.S.; Shui, L.; Jin, M.; Yi, Z.; Yuan, M.; Li, N.; Yang, X.; et al. First-Principles Study of Optoelectronic Properties of the Noble Metal (Ag and Pd) Doped BiOX (X = F, Cl, Br, and I) Photocatalytic System. *Catalysts* **2019**, *9*, 198. [CrossRef]
20. Zhang, H.; Yang, Y.; Zhou, Z.; Zhao, Y.; Liu, L. Enhanced Photocatalytic Properties in BiOBr Nanosheets with Dominantly Exposed (102) Facets. *J. Phys. Chem. C* **2014**, *118*, 14662–14669. [CrossRef]
21. Wang, Y.; He, J.; Zhu, Y.; Zhang, H.; Yang, C.; Wang, K.; Wu, S.-c.; Chueh, Y.-L.; Jiang, W. Hierarchical Bi-doped BiOBr microspheres assembled from nanosheets with (001) facet exposed via crystal facet engineering toward highly efficient visible light photocatalysis. *Appl. Surf. Sci.* **2020**, *514*, 145927. [CrossRef]
22. Mi, Y.; Li, H.; Zhang, Y.; Du, N.; Hou, W. Synthesis and photocatalytic activity of BiOBr nanosheets with tunable crystal facets and sizes. *Catal. Sci. Technol.* **2018**, *8*, 2588–2597. [CrossRef]
23. Wu, X.; Ng, Y.H.; Wang, L.; Du, Y.; Dou, S.X.; Amal, R.; Scott, J. Improving the photo-oxidative capability of BiOBr via crystal facet engineering. *J. Mater. Chem. A* **2017**, *5*, 8117–8124. [CrossRef]
24. Li, H.; Hu, T.; Du, N.; Zhang, R.; Liu, J.; Hou, W. Wavelength-dependent differences in photocatalytic performance between BiOBr nanosheets with dominant exposed (001) and (010) facets. *Appl. Catal. B Environ.* **2016**, *187*, 342–349. [CrossRef]
25. Zhang, X.; Li, W.; Hu, L.; Gao, M.; Feng, J. A Tight-Connection g-C_3N_4/BiOBr (001) S-Scheme Heterojunction Photocatalyst for Boosting Photocatalytic Degradation of Organic Pollutants. *Nanomaterials* **2024**, *14*, 1071. [CrossRef] [PubMed]
26. Yu, Q.; Chen, J.; Li, Y.; Wen, M.; Liu, H.; Li, G.; An, T. In-situ decoration of metallic Bi on BiOBr with exposed (110) facets and surface oxygen vacancy for enhanced solar light photocatalytic degradation of gaseous n-hexane. *Chin. J. Catal.* **2020**, *41*, 1603–1612. [CrossRef]
27. Jia, W.; Peng, D.; Feng, Z.; Wu, X.; Liu, Y.; Zheng, X.; Yuan, X. UV-light-assisted green preparation of Bi/BiOBr/RGO composites with oxygen vacancies toward enhanced photocatalytic removal of organic dye. *New J. Chem.* **2020**, *44*, 7749–7757. [CrossRef]
28. Cao, F.; Wang, J.; Wang, Y.; Zhou, J.; Li, S.; Qin, G.; Fan, W. An in situ Bi-decorated BiOBr photocatalyst for synchronously treating multiple antibiotics in water. *Nanoscale Adv.* **2019**, *1*, 1124–1129. [CrossRef]
29. Zheng, C.; Cao, C.; Ali, Z. In situ formed Bi/$BiOBr_xI_{1-x}$ heterojunction of hierarchical microspheres for efficient visible-light photocatalytic activity. *Phys. Chem. Chem. Phys.* **2015**, *17*, 13347–13354. [CrossRef]
30. Mishra, S.; Acharya, R. Recent updates in modification strategies for escalated performance of Graphene/MFe_2O_4 heterostructured photocatalysts towards energy and environmental applications. *J. Alloys Compd.* **2023**, *960*, 170576. [CrossRef]
31. Chen, X.; Zhao, B.; Ma, J.; Liu, L.; Luo, H.; Wang, W. The BiOBr/Bi/Bi_2WO_6 photocatalyst with SPR effect and Z-scheme heterojunction synergistically degraded RhB under visible light. *Opt. Mater.* **2021**, *122*, 111641. [CrossRef]
32. Wu, M.; Dong, M.; El-Bahy, Z.M.; Jing, T.; Mersal, G.A.M.; Tian, J.; Qi, H.; Shi, D.; Naik, N.; Murugadoss, V.; et al. Preparation of Bi/BiOBr sensitized titania nanorod arrays via a one-pot solvothermal method and construction of kanamycin photoelectrochemical aptasensors. *Dalton Trans.* **2022**, *51*, 8279–8289. [CrossRef]
33. Donohue, M.D.; Aranovich, G.L. Classification of Gibbs adsorption isotherms. *Adv. Colloid Interface Sci.* **1998**, *76–77*, 137–152. [CrossRef]
34. Kruk, M.; Jaroniec, M. Gas Adsorption Characterization of Ordered Organic−Inorganic Nanocomposite Materials. *Chem. Mater.* **2001**, *13*, 3169–3183. [CrossRef]
35. Hao, J.; He, H.; Gong, S.; Fan, J.; Xu, Q.; Min, Y. WN Coupled with Bi Nanoparticles to Enhance the Localized Surface Plasmon Resonance Effect for Photocatalytic Hydrogen Evolution. *ACS Appl. Mater. Interfaces* **2021**, *13*, 19884–19893. [CrossRef]
36. Qin, M.; Jin, K.; Li, X.; Wang, R.; Zhao, Y.; Wang, H. Bi nanosphere-decorated oxygen-vacancy BiOBr hollow microspheres with exposed (110) facets to enhance the photocatalytic performance for the degradation of azo dyes. *New J. Chem.* **2022**, *46*, 12410–12418. [CrossRef]
37. Sun, C.; Zhao, Z.; Fan, H.; Chen, Y.; Liu, X.; Cao, J.; Lang, J.; Wei, M.; Liu, H.; Yang, L. Oxygen vacancy induced electron traps in tungsten doped Bi_2MoO_6 for enhanced photocatalytic performance. *CrystEngComm* **2021**, *23*, 7270–7277. [CrossRef]
38. Guo, Y.; Wen, H.; Guo, Y.; Ruan, J.; Huang, H.; Peng, J.; Lin, Z.; Dong, H. Surface states modulation via vacancy engineering for creating band bending on semiconductor BiOBr photocatalysts. *Colloids Surf. A Physicochem. Eng. Asp.* **2024**, *682*, 132915. [CrossRef]